Thermal variations in the mantle inferred from 660 km discontinuity topography and tomographic wave speed variations

George Helffrich

Earth and Planetary Science, Tokyo Institute of Technology, 2-12-1 Ookayama, Meguro-ku, Tokyo 152-8551, Japan * *E-mail: george@bristol.ac.uk*

SUMMARY

Variations in mantle temperatures cause changes in seismic wave speeds and changes in the pressure at which mineralogical reactions occur, changing the depth at which a seismic discontinuity occurs. As an experiment in using global seismological data sets in a statistical way to draw inferences concerning the Earth using angular correlation functions, we analyse wave speed variations in *P*- and *S*-wave tomographic studies and perturbations to the depth of the 660 km discontinuity, with the goal of inferring lateral temperature variations in the lower mantle. On account of discrepancies between the temperatures estimated using various data sets, the results are not particularly encouraging. We find variations in temperatures of 60 or 90–120 K at the top of the lower mantle, depending on the data set used, 60 K in the middle of the lower mantle, and potentially 60 or 300 K in the core–mantle boundary region. Based on 660 km depth perturbations, plumes might be 160 K warmer than the ambient lower mantle. Future improvements in angular correlation analyses could be obtained through finer gridding of the global data sets.

Key words: angular correlation functions, core–mantle boundary, mantle discontinuities, mantle structure, mantle temperatures.

1 INTRODUCTION

Secular cooling and internal heat production in the Earth causes solid-state convection in the mantle, the surface expression of which is the motion of the plates and the diversity of geographical and geological features related to plate boundary interactions. The heat is not expelled uniformly across the surface of the planet, but varies with position, which suggests temperature differences at depth in the mantle, such as those caused by cratonic roots, mid-ocean ridge melting and intraplate volcanism. Interpreting the surface heat flux as lateral mantle temperature variations is confounded by the uneven distribution of heat-producing elements in the crust and a possible tectonic component caused by strain heating (Jaupart *et al.* 1998; Kincaid & Silver 1996). An alternative way to study lateral variations in mantle temperatures is to work with observable characteristics of the mantle at depth and to use them for *in situ* mantle thermometry.

Seismological studies provide at least two different ways of investigating mantle temperature variations. One way is through the effect that temperature changes have on seismic wave speeds. One can transform the wave speed variations found in tomographic studies of the mantle (Grand 1994; van der Hilst *et al.* 1997) into temperature variations using the high-pressure temperature dependence of

*Now at: Earth Sciences, University of Bristol, Bristol BS8 1RJ, UK.

the bulk and shear moduli (Bina & Helffrich 1992; Ita & Stixrude 1992; Chopelas *et al.* 1994). With this approach, however, there are three problems. The first is that the temperature dependence of the shear modulus at high pressure has not been verified experimentally, and may differ from the theoretical prediction. Secondly, there is an unknown component in the wave speed variations caused by compositional changes in the mantle material. Finally, the effect of minor amounts of partial melt on shear moduli is poorly understood, and melt may be present in some regions of the mantle near ridges, hotspots and possibly at the core–mantle boundary (CMB). Therefore, the results should be viewed as conditional on the assumptions of a correct theory for the shear modulus, compositional homogeneity in the mantle and no melt being present. The first of these assumptions is empirically justified at low pressures (Anderson *et al.* 1991) and there is no *a priori* reason to believe that high pressure renders it incorrect. The second assumption is less strongly justified because small-scale compositional heterogeneities demonstrably exist in the mantle (Kaneshima & Helffrich 1999). They are probably widely dispersed in the mantle, however, and make up less than approximately 15 per cent of the mantle (Helffrich & Wood 2001), but possibly a locally larger fraction of the base of the mantle. Neglecting their impact on large-scale wave speed variations in the lower mantle except near the CMB seems justified. The most drastic assumption is the neglect of partial melt effects on the shear wave speeds. The solidus of the lower mantle appears to be at much higher temperatures than is plausible for

2   *G. Helffrich*

lower-mantle adiabats except at the CMB (Zerr *et al.* 1998), where other seismological investigative methods suggest extremely large wave speed variations (Garnero *et al.* 1998). Interpreting wave speed variations here as having an exclusively thermal origin is probably wrong, and the results should only be viewed as lower bounds on temperature variations.

Another seismological technique provides a cross-check on tomographically based temperature estimates at some mantle depths, however. Because the seismic discontinuities at depths of 410 and 660 km demark mantle phase transitions, the depths of which depend on the ambient temperature through the Clapeyron slopes of the respective reactions (Fei *et al.* 1991; Bina & Helffrich 1994; Helffrich 2000), their lateral depth changes provide an independent estimate of thermal variations in the mantle. At the depths of the seismic discontinuities one can therefore compare the thermal variability estimates as a cross-check. Since they presumably measure the properties of the same earth, any differences in results signify departures in the earth from the assumptions discussed previously. The goal remains, however, to use the lateral changes in seismic properties to infer lateral temperature variations at different mantle depths.

Exploring the lower mantle for temperature variations is riskier because the absence of visible discontinuities there thwarts the cross-checking ability provided by the 660 km discontinuity at the top boundary of the lower mantle. In this region, *P*- and *S*-wave tomography studies provide the only check on temperature estimates through their mutual consistency. One explanation for the variations in the structure of D″, the region just above the CMB, is lateral variations in its temperature (Loper & Lay 1995). Based on mineral stability calculations, however, some think part of the structure in D″ may be caused by a phase transition in SiO_2 (Karki *et al.* 1997) or a perovskite decomposition to $MgO + SiO_2$ (Knittle & Jeanloz 1991; Saxena *et al.* 1996), the Clapeyron slope of which might provide an independent reckoning of temperature. There is, however, little experimental support for such a transition, with most experimental attempts at detecting stishovite or perovskite breakdown yielding negative results (Kesson *et al.* 1998; Serghiou *et al.* 1998).

The approach taken here will be to compare inferred temperature variations from global *P*- and *S*-wave tomographic studies with those obtained through an analysis of global 660 km discontinuity depths at the top of the lower mantle. In the middle and the bottom of the lower mantle, the global tomographic studies provide the only temperature estimates. There are limitations inherent in the data used in this approach that will be discussed in the following sections. This effort is an attempt to introduce a statistically based analysis method to whole-earth data to draw inferences concerning its physical state. Any weaknesses in the data sets used will hopefully alert future analysts to ways of providing data that facilitate spatial analysis at higher statistical levels of confidence.

2 DATA, METHODS AND LIMITATIONS

We use data from Flanagan and Shearer's (1998) study of global 660 km discontinuity depths using precursors to *SS*. The point estimate data are binned and averaged, with each bin being separated by ∼10° at the Earth's surface and smoothed over 20° wide regions. We also use data from Grand's (1994) shear wave tomographic study and van der Hilst *et al.*'s (1997) compressional wave study, both of which provide wave speed perturbations from a radial earth reference model in 2×2 deg² blocks at ≈ 250 km depth intervals from the surface to the CMB.
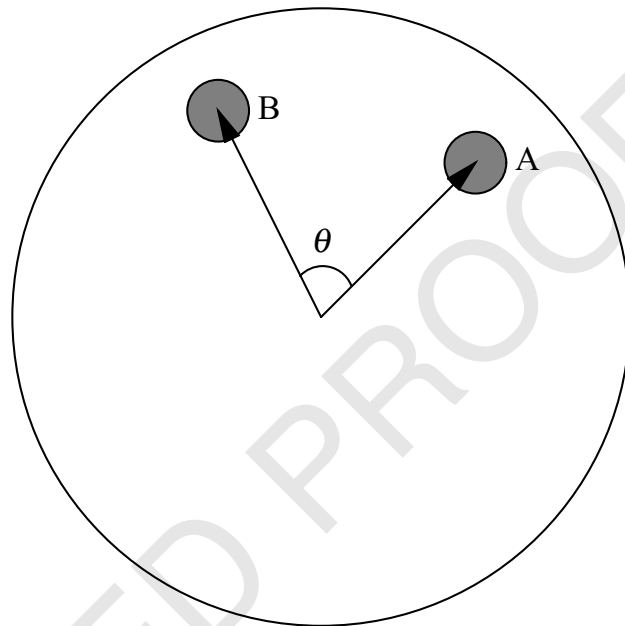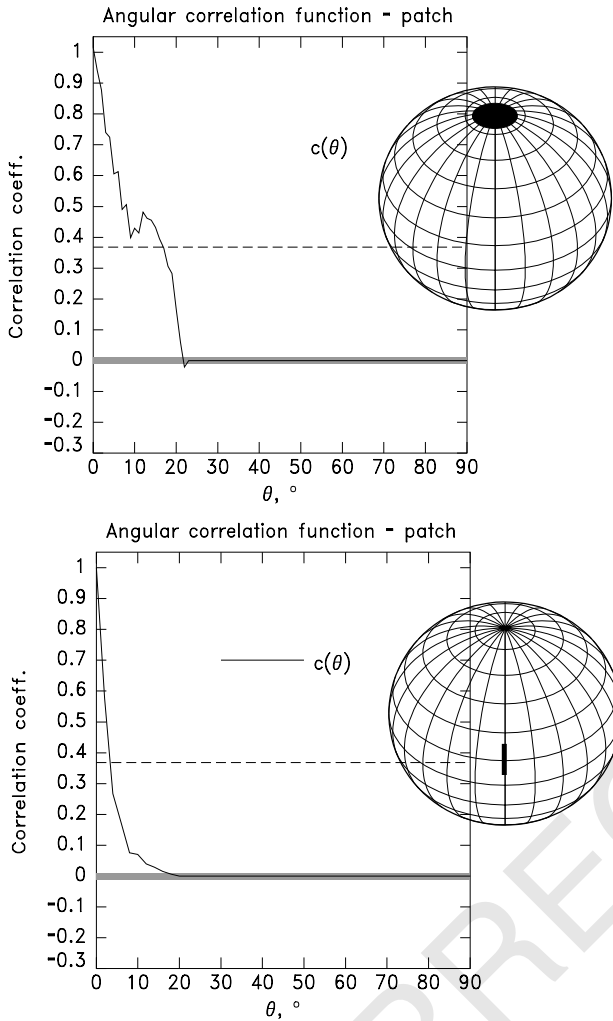

Figure 1. The angular correlation function associates a pair of points on a sphere A and B, and measures their correlation. θ is the angle separating A and B. There are many points on the sphere at the same angular separation. The correlations between all unique pairs separated by θ yields the value of the correlation function $c(\theta)$, which ranges from +1 to −1. $c(0) \equiv 1$ because there every point on the sphere is perfectly correlated with itself. The correlation function $c(\theta)$ represents the fractional variance in the data that is attributable to processes acting at an angular separation of θ.

The main analysis tool is the angular correlation function of these data sets. This function indicates how correlated neighbouring data points are on a spherical surface (Fig. 1). The metric defining the correlation neighbourhoods is the angular distance separating two points on the sphere. Every point is perfectly correlated with itself, yielding unit correlation at zero separation. With greater separation we expect a correlation decrease, eventually reaching some distance where the function values at those points are no longer related to each other. At this separation, the values are uncorrelated, with a zero correlation coefficient. Anticorrelation is possible if the entire spherical field has structure such as prescribed by spherical harmonics of positive degree. Diametrically opposite points in a degree-one field would be inversely correlated with each other, for example. Angular correlation functions are commonly used in astronomy for studying the clustering of mass in the Universe (Peebles 1980) and the blackbody microwave background radiation remaining from the initial expansion of the Universe (Levi 1992).

The correlation function responds to the shape of a feature in a statistical way, emphasizing the most frequently encountered combinations of properties. The correlation length of an equant patch is approximately its diameter (Fig. 2). In contrast, the correlation function of an elongate patch emphasizes its width. This is because there are many more points at short separations that make up the patch than there are at larger separations, which are restricted to being along its length.

Dividing the data into distance bins (1° for tomographic and 10° for topographic data) is the first step in calculating the angular correlation function. For every pair (a_i, b_i) of N points at a distance θ, the correlation coefficient is

Angular correlation function – patch

Angular correlation function – patch

Figure 2. Angular correlation function $c(\theta)$ for two test cases: a $10°$ radius spherical cap (top) and a $4 \times 20°$ rectangle (bottom) to illustrate their appearance in an angular correlation function. A horizontal dashed line marks the e^{-1} correlation length, the separation distance where properties are no longer significantly correlated with one another. $c(\theta)$ for the equant cap is significantly correlated out to separations of $17°$, nearly the diameter of the cap, and zero from $20°$ onwards. Thus, $c(\theta)$ is principally sensitive to the spread of an equant patch. In contrast, angular correlation function of the elongate, rectangular patch drops to insignificant values at $3°$, approximately the width of the object, because there are many more points on it at small separations than at large ones. The grey band indicates the 95 per cent confidence level of a non-zero correlation determined by a *t*-test.

$$c(\theta) = \frac{\sum_i^N [w_i(a_i - \mu)][w_i(b_i - \mu)]}{\sqrt{\left[\sum_i^N w_i^2(a_i - \mu)^2\right]\left[\sum_i^N w_i^2(b_i - \mu)^2\right]}}, \qquad (1)$$

where μ is the mean of all the data and w_i is a weight factor. A *t*-test for a non-zero mean value gives the 95 per cent confidence limits for c shown in figures depicting angular correlation plots. (Owing to the large numbers of pairs of points in the tomographic data sets, these are quite narrow.) The observational data do not always sample the sphere uniformly, particularly if they are reported at uniformly spaced points in latitude λ and longitude ϕ, which oversample the polar areas. To homogenize the sampling, each data

point is weighted by $w_i = \cos \lambda_i$ and the mean in eq. (1) is calculated by $\mu = (\sum_i^N w_i a_i)/(\sum_i^N w_i)$.
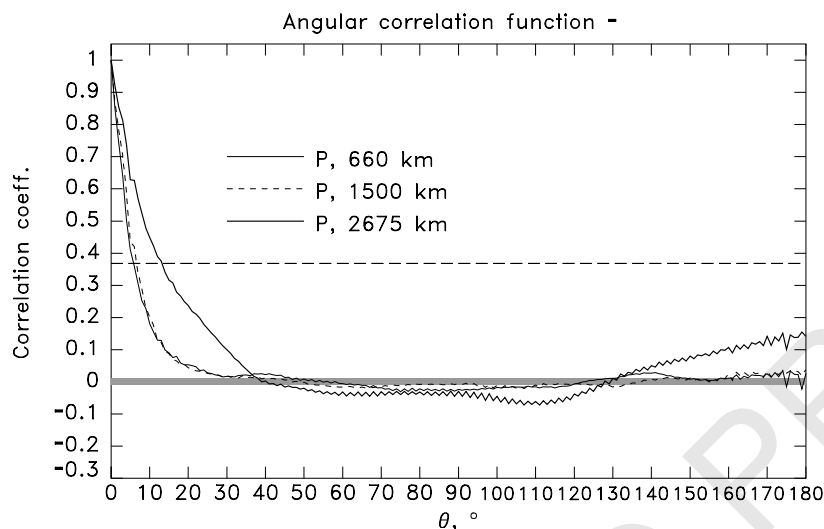
An angular correlation function provides two types of information concerning the data distribution. The first is the overall shape of the correlation function, and how this varies with depth. Since the anticipated lateral thermal variations in the mantle should decay exponentially with distance, we expect to see a relatively steep decay from the unit peak at zero separation distance if they are conductive. In the ≈ 10–30 Myr transit time across the depth of the mantle by sinking slabs or rising plumes (Larson & Olson 1991), not much conductive decay will occur, affecting at most a distance $d = \sqrt{\kappa t}$ around the thermal mass. For a mantle thermal diffusivity $\kappa = 1 \times 10^{-6}\,\mathrm{m^2\,s^{-1}}$ and $t = 20$ Myr, this is ≈ 25 km – not much larger than the slab or plume width itself (100–200 km). Thus the dominant component to the spatial variation should be the dimension of the rising or sinking thermal mass itself, allowing for a factor of 2 greater width caused by long-term subduction or plume ascent in a single region. There will also be broadening of the features as they pass into the lower mantle caused by its higher viscosity by approximately the same amount.

In addition to the lateral scale of spatial property variation, the magnitude of the correlation represents the fraction of the data variance contributed by a process acting at that distance (Jenkins & Watts 1968). Thus in seismic wave speed variations we would expect to see the effect of a 100 km thick slab of subducted lithosphere at lengths of ~ 0.5–$1°$ and with a correlation coefficient close to maximum, since slab/mantle temperature differences are the largest anticipated in the mantle (800 K difference, Furukawa 1994). On the other hand, plume conduit diameters are probably ≈ 200 km wide in the upper mantle (Sleep 1992), and have temperature differences of ~ 200 K relative to the mantle, so it would contribute to the variance at $(200/800)^2$ or $1/16$ the maximum at a $1°$–$2°$ separation.

The processing methods associated with the observational data impose limitations on the conclusions that may be drawn from the analyses to follow. The first methodological aspect is the binning and smoothing that is applied to the discontinuity topography point estimates. They are smoothed over $20°$ patches separated by $10°$ (Flanagan & Shearer 1998). This will induce correlations at larger separations than the raw data may contain. However, the smoothing dimension is selected to mimic the Fresnel zone size of *SS* at its bounce point and thus represents the natural averaging inherent in the data.

The second aspect warranting caution arises from the damping or regularizations applied in traveltime data inversions for structure. These tend to favour longer-wavelength structure. There is also the choice of block sizes into which the earth is divided for the inversion. Practitioners select this based on the resolving power of the data through spike or checkerboard resolution tests, and structures smaller than this cannot be retrieved with confidence (van der Hilst *et al.* 1993; Grand 1994). Thus, short-wavelength features will be muted. However, thin, high-velocity features corresponding to subducted lithospheric slabs are featured in tomographic inversions, so short-wavelength features can persist if so required by the data.

Finally, traveltime-based studies are not very sensitive to velocity structure immediately below a seismic discontinuity because the rays turning there are never first arrivals. Under the assumption that temperature variations extend vertically at the scale of the tomographic model layer thickness—as we expect slabs and plumes to do—this effect may not completely prevent the structure below a discontinuity being interrogated.

4   *G. Helffrich*

Figure 3. Angular correlation function $c(\theta)$ of tomographic *P*-wave speed variations (van der Hilst *et al.* 1997) relative to IASP91 at three depths in the mantle: below 660 km, at 1500 km, and at the core–mantle boundary. The grey band gives the 95 per cent confidence level that $c(\theta)$ is non-zero. A horizontal dashed line marks the e^{-1} correlation length, the separation distance where wave speed variations are no longer significantly correlated with one another. The decorrelation distance is the separation at which $c(\theta)$ goes to zero. The correlation length is $\approx 7°$ at the top and middle of lower mantle and broadens somewhat to $14°$ at the base. The decorrelation distance is $\sim 35°$ at all levels.

3 RESULTS

3.1 *P* angular correlation

Fig. 3 shows the angular correlation function of *P*-wave velocities from a tomographic study by van der Hilst *et al.* (1997) at three levels in the lower mantle: the top, just below the 660 km discontinuity; the middle, centred at 1500 km depth; and the base, just above the CMB.

The figure shows that a change in structure with depth occurs at the base of the mantle, but it is not dramatic. The correlation length, defined by a drop to e^{-1} (≈ 0.37) of its maximum, is $\sim 7°$ at the top and the middle of the mantle, but expands to $\sim 14°$ at the bottom of the mantle. However, since the arc length of a degree shrinks with depth by the ratio of radii, the geometric factor makes the correlation length increase only by a factor of 1.3, or from approximately 750 to 1000 km throughout the mantle. The distance at which the correlation first crosses zero (called the decorrelation length here) is approximately constant with depth at $35° \pm 5°$ from 660 km to the CMB. It hovers at levels nearly indistinguishable from zero at the 95 per cent confidence level in this distance range, so there is little use in interpreting it more closely. Curiously, in the lowermost mantle, there is a significant antipodal velocity correlation, resolvably different from zero at better than four times the 95 per cent confidence level.

At 90°, wave speeds correlate negatively, a pattern most clearly shown at the top and bottom of the mantle. The negative correlation region is centred at 90° in a $\pm 45°$ band (possibly wider at the CMB), indicating a degree-two spherical harmonic pattern that others have reported in tomographic images (Dziewonski & Woodhouse 1987; Su & Dziewonski 1992).

At 660 km, the variance in *P* is 4.59×10^{-6} in fractional velocity change, at 1500 km it is 2.81×10^{-6} and at the CMB it is 5.98×10^{-6}. The associated wave speed variation at the correlation length is $\sqrt{4.59 \times 10^{-6} \times e^{-1}}$ or 0.13 per cent below 660 km, 0.10 per cent at 1500 km depth, and 0.15 per cent at the CMB.

3.2 *S* angular correlation

In a similar way to the previous figure, Fig. 4 shows the angular correlation function of *S*-wave velocities from a tomographic study by Grand (1994) at the same three mantle levels. Though the overall shape of the angular correlation function is similar, it is substantially different in the amplitude of the negatively correlated region around 90° and in the more systematic lengthening of the correlation length with depth.

The correlation length extends from 5° at the top of the lower mantle to 9° at ≈ 1500 km depth and greatly expands to 24° at the CMB. Similarly, at the top of the lower mantle, the decorrelation distance is 30°, roughly equivalent to *P*. Deeper in the lower mantle it systematically expands to 45° at ≈ 1500 km and 55° at the CMB.

The variance in the *S*-wave speeds is 2.23×10^{-6} at 660 km, 2.25×10^{-6} at 1500 km and 1.32×10^{-4} at the CMB. This corresponds to $\sqrt{2.23 \times 10^{-6} \times e^{-1}}$ or a 0.09 per cent wave speed difference just below 660 km, 0.09 per cent at 1500 km, and an enormous 0.70 per cent difference at the CMB.

The degree-two pattern is also evident in the *S*-wave speed variations but is more pronounced. A region of negative correlation extends $\pm 30°$ around 90°. The variance associated with the negative peak at 90° at the level of the CMB is -0.15 of the maximum of 1.32×10^{-4} fractional wave speed variation, or accounts for a 0.45 per cent wave speed perturbation. The rise in $c(\theta)$ at antipodal distances is also consistent with a degree-two pattern.

3.3 660 km discontinuity depth angular correlation

On account of the larger bin size in Shearer's (1993) discontinuity study (also adopted by Flanagan & Shearer 1998), there are many fewer point estimates of discontinuity depths. The coarser resolution is evident in Fig. 5 in the size of the 95 per cent confidence level for a non-zero correlation. Only at distances less than $\approx 15°$ is the correlation level different from zero. The correlation
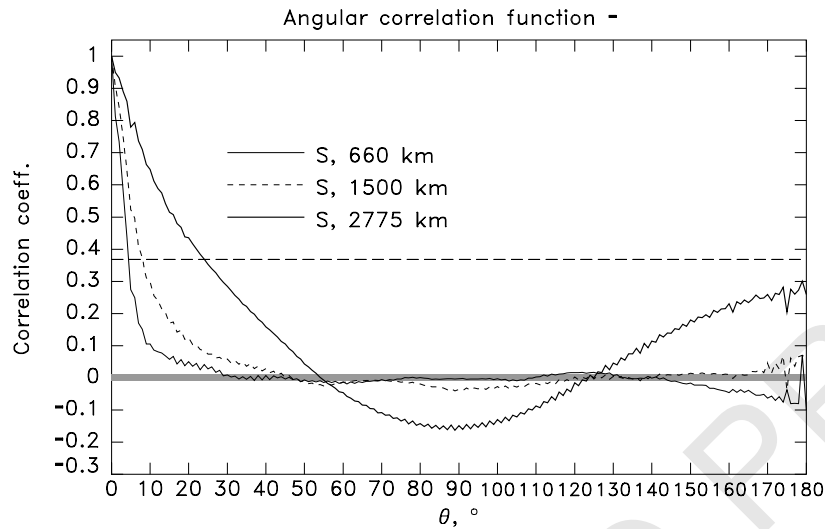
Figure 4. Angular correlation function $c(\theta)$ of tomographic *S*-wave speed variations relative to a continental or oceanic reference model (Grand 1994) at three depths in the mantle: below 660 km, at 1500 km and at the core–mantle boundary. The grey band gives the 95 per cent confidence level that $c(\theta)$ is non-zero. A horizontal dashed line marks the e^{-1} correlation length, the separation distance where wave speed variations are no longer significantly correlated with one another. The decorrelation distance is the separation at which $c(\theta)$ goes to zero. The correlation length is 5° at the top of the lower mantle, expands to 9° in the middle of the lower mantle, and 24° at the CMB. The decorrelation distance is similarly increases from 30° to 45° and then to 55° in the lower mantle.
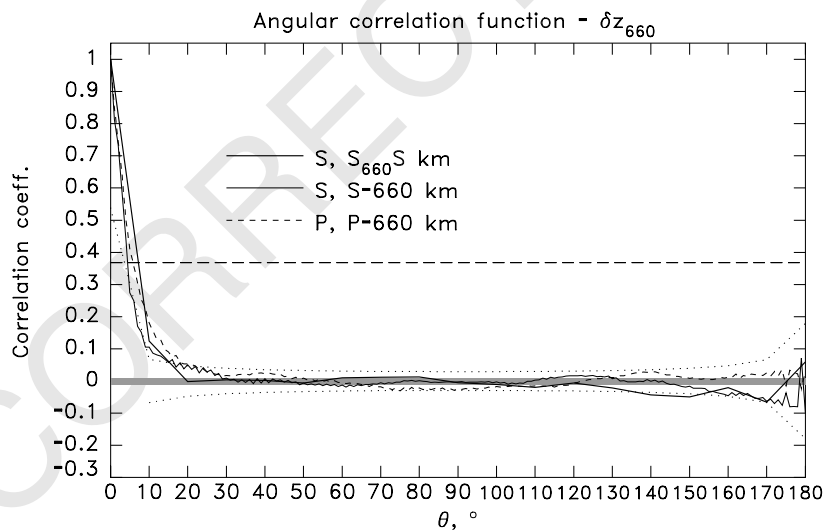
Figure 5. Angular correlation function $c(\theta)$ of global 660 km discontinuity depths obtained through analysis of precursors to *SS* (Flanagan & Shearer 1998), and the tomographic *P*- and *S*-wave speed perturbations just below 660 km depth in the lower mantle shown in the previous two figures. The dotted line gives the 95 per cent confidence level that $c(\theta)$ is non-zero. The horizontal dashed line marks the e^{-1} correlation length, the separation distance where wave speed variations are no longer significantly correlated with one another. The decorrelation distance is the separation at which $c(\theta)$ goes to zero. The correlation length is $\approx 4°$ based on exponential interpolation of the first few $c(\theta)$ values. By comparison with the tomographic studies there are many fewer depth estimates, leading to a rougher appearance of the correlation function and few distances where $c(\theta)$ is non-zero with 95 per cent confidence. The grey band demarks the 95 per cent confidence level for a non-zero correlation for the tomographic studies.

length is smaller than the bin size, and interpolating exponentially using the first three $c(\theta)$ points yields an approximate correlation length of 3.5°. Similarly interpolated, the decorrelation distance is 11°. On account of there not being well-characterized discontinuities deeper in the mantle, there are no comparisons with the correlations deeper in the mantle such as the tomographic studies provide.

4 INTERPRETING ANGULAR CORRELATION FUNCTIONS

4.1 Wave speed variations

Some way to translate these characterizations of the spatial property variations in both *P*- and *S*-wave velocities and 660 km discontinuity

6   *G. Helffrich*

depths into mantle temperature changes is required. Assuming the tomographic variations are caused by lateral variations in temperature, we need the appropriate scaling relation between the velocity change ΔV and the temperature change ΔT, valid at lower-mantle pressures. The correlation lengths provide the variance to be explained at that distance, which is around a 0.1 per cent change in P and S velocities. Thus the task is to calculate how large a temperature change from a reference geotherm would give those velocity variations. The chief uncertainty in this method is how the shear modulus μ responds to temperature changes at lower-mantle pressures, owing to the fact that it appears in both velocities,

$$V_p = \sqrt{K/\rho + \frac{4}{3}\mu/\rho}, \quad V_s = \sqrt{\mu/\rho}, \quad (2)$$

along with the adiabatic bulk modulus K and the density ρ. With present techniques, lattice dynamic simulations of elastic properties provide a feasible means to calculate microsecond time-scale behaviour (Gale 1997) to a computationally practical theory level. Fitting calculated elastic moduli along isotherms to a Birch–Murnaghan model and the temperature dependence of the moduli at zero pressure to a constant δ_T and $\eta = -(\alpha\mu)^{-1}\,d\mu/dT$ models, we capture the high-pressure and high-temperature moduli dependence. For a description of the calculation method, see Bina & Helffrich (1992).

Fig. 6 displays the calculated seismic wave speed dependence on temperature at the mantle depths of interest. With increasing depth, the effect of temperature lessens: a larger temperature change is
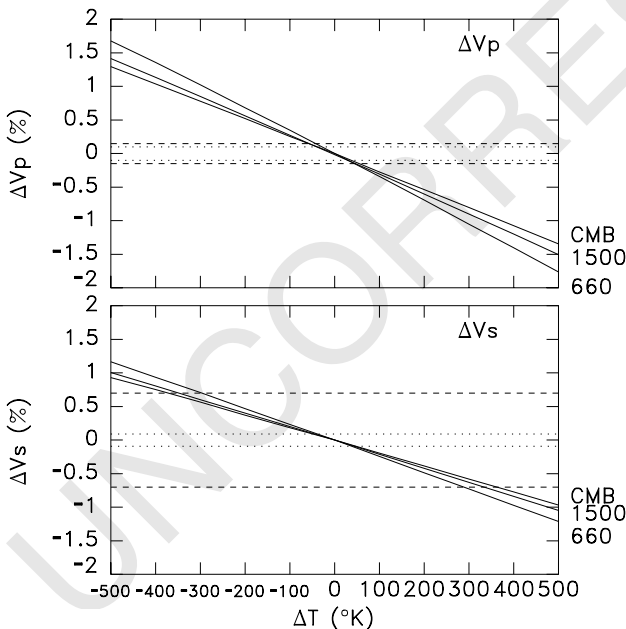
Figure 6. Calculated wave speed variations caused by temperature changes at three lower-mantle depths: below 660 km, at 1500 km and at the CMB. The lower-mantle mineralogy is 6 vol. per cent $CaSiO_3$ perovskite, 72 vol. per cent $(Mg, Fe)SiO_3$ perovskite and 22 vol. per cent $(Mg, Fe)O$ magnesiowüstite. Temperatures are relative to an adiabat initiated at 1950 °C below the 660 km discontinuity. Horizontal dashed lines show temperature perturbations required to explain the variance in the tomographic P- and S-wave speed variations at all depths for P (top, 0.10–0.15 per cent) everywhere in the lower mantle and for S (bottom, 0.09 per cent) at the top and middle of the lower mantle, all $\sim \pm 60$ K. At the CMB, the S-wave speed variations are 0.70 per cent, requiring $\sim \pm 375$ K temperature difference.

needed to change wave speeds by the same amount. For example, a 1 per cent change in P-wave speed is produced by a 300 °C temperature change at the top of the lower mantle, but a 400 °C change at the CMB. (This results from the dual impact of thermal expansivity on both K and ρ in V_p, while principally affecting only ρ in V_s.) At the correlation length, the P-wave speed variation ($\sqrt{\text{variance}}$) is 0.13 per cent at the top, dropping slightly to 0.10 per cent in the middle of the lower mantle and 0.15 per cent at the bottom of the lower mantle. This corresponds to ± 60 K temperature variations throughout the mantle. The S-wave speed variations behave similarly at the top and middle of the lower mantle: the 0.13–0.10 per cent variation at the top and middle of the mantle yield temperature change estimates of ± 60 K as well. The bottom of the lower mantle looks very different to S waves, however, with $\sim \pm 300$ K temperature changes being required. Since we are using the same level of theory to account for temperature changes in the bulk and shear moduli, this discrepancy strongly suggests that some process other than lateral temperature variations changes the shear modulus properties in D″, as others have also concluded (Kennett *et al.* 1998). Elsewhere in the lower mantle, ± 60 K lateral temperature variations explain the variability in seismic wave speeds observed in tomographic studies.

4.2 Discontinuity depth estimates

There is substantially more uncertainty in interpreting discontinuity depths owing to the method used to estimate them. These are caused by wave propagation effects involving *SS*. While Shearer (1993) notes that the Fresnel zone of *SS* is large at its bounce point and uses its approximate size for spatially binning and averaging individual observations, Chaljub & Tarantola (1997), and Neele *et al.* (1997) showed that biases still remain. By calculating synthetic seismograms from known discontinuity topographies and analysing the seismograms to infer the discontinuity depths in the same way as Shearer (1993) did, they found that small-scale topography on the discontinuities was not successfully retrieved. Neele *et al.* (1997) found that both the magnitude of the topography was always underestimated and the sign of the topography was opposite to its actual value under some conditions. Chaljub & Tarantola (1997) did a similar study with a different method for generating the synthetic seismograms and explored the biases of the method more systematically. Similarly to Neele *et al.* (1997), they found that the method yielded estimated topography with the wrong sign if it had short, 800 km wavelengths. Larger than 2500 km, either uplifted or depressed topography is properly retrieved, and uplifted topography when wider than 1500 km. Estimates appear biased to smaller deviations at wavelengths shorter than 2500 km for depressed topography and at 1500 km for uplifted topography. Since the *SS* topography features are all narrower than these limits, they must be corrected for bias before being interpreted as characteristics of the mantle. To correct for the bias in depressed topography, Chaljub and Tarantola's (1997) results may be approximately summarized by observing that the apparent depths h_{app} decay to e^{-1} from their true depths h_t in approximately 1700 km. The corrections for uplifted topography are not as systematic, but they may similarly be parametrized by an e^{-1} decay in 900 km. Thus, at a correlation distance θ at radius r km in the mantle,

$$h_t \approx h_{\text{app}} \exp(\max[0, (b - r\theta)/d]), \quad (3)$$

where the constants (b, d) are (2500, 1700) for depressed topography and (1500, 900) for uplifted topography.

The *SS* topography correlation length is approximately 3.5°. Assuming this is caused by equal amounts of uplift and depression on the discontinuity, at 350 km scales (3.5° at 660 km) h_t is $3.54 h_{app}$ if uplifted and $3.58 h_{app}$ if depressed. Thus an average correction factor of 3.56 for the apparent depths seems appropriate. The depth variance to be explained at the correlation length is $\sqrt{62.2 \times e^{-1}}$ or 4.78 km. The unbiased depth variation is therefore 4.78×3.56 or 17.1 km. Using the spherical earth relation $dP/dz = \rho g/3$ with $\rho = 4240$ kg m^{-3}, $g = 9.81$ m s^{-2}, and a Clapeyron slope dP/dT of -2 MPa K^{-1} (Bina & Helffrich 1994), one calculates

$$\delta T = \delta z \times dP/dz \times (dP/dT)^{-1}. \qquad (4)$$

This corresponds to $\approx \pm 120$ K variations in temperature at the correlation length.

5 DISCUSSION

5.1 Top of the lower mantle

At the top of the lower mantle, where wave speed variations in both *P*, *S* and topographic variations on the 660 km discontinuity are available, similar views of the mantle emerge. *P*- and *S*-wave speed variations both suggest temperature differences of ± 60 K, whereas the 660 km topography variance suggests temperature differences of approximately double this value, ± 120 K.

The agreement is not particularly good, and may in part be caused by the large grid on which the estimates are provided, forcing the correlation length to be estimated by interpolation. Another cause may be the way in which the methods sample the vicinity of the discontinuity. In the earlier discussion of the limitations of the data sets, the poor sensitivity of traveltime data to structure just below discontinuities was noted. In contrast, *S* precursors give information concerning the discontinuities near the bounce point and nowhere else—the precursory arrival from the reflection from 660 km would not be present without the discontinuity. However, the Fresnel zone at the *SS* bounce point is 2000 km wide, which is approximately the smoothing size in these studies (Shearer 1993; Flanagan & Shearer 1998). Thus, while *SS* precursors give information at precisely the depth where it is desired, it represents a lateral average of 660 km properties in a region 2000 km wide surrounding the bounce point. Topographic deflections caused by cold, subduction zone slabs sinking through 660 km might dominate the *SS* precursor signal, since these are the largest thermal variations we expect in the mantle. The impact of this factor on the results is worth assessing.

One way to check for the influence of subduction zones is by excluding any bounce points close to convergent plate boundaries. The uncertainty in the resulting two-point correlation function depends on the exclusion distance, as shown in Fig. 7, but not strongly. At exclusion distances of 14° or more, the variance drops to values between 45 km^2 as compared with 62.2 km^2 in the full data set. Excluding points within 20° of a convergent boundary, so that the smoothing applied to the raw data will not include bounce points in that region, the correlation length is $\approx 4.5°$ and the data variance is 45.67 km^2. Correcting for the bias for this ≈ 450 km wavelength (factors of 3.34–3.21, or 3.27 on average) leads to elevation differences away from subduction zones of 13.4 km, requiring temperature differences of $\sim \pm 90$ K. The discrepancy between tomographic and topographic temperature estimates is now slightly diminished, but subduction zones do not appear to dominate the signature of discontinuity topography.

Hotspots avoid subduction zones (Weinstein & Olson 1989), so the variance of the data excluding convergent plate boundaries con-
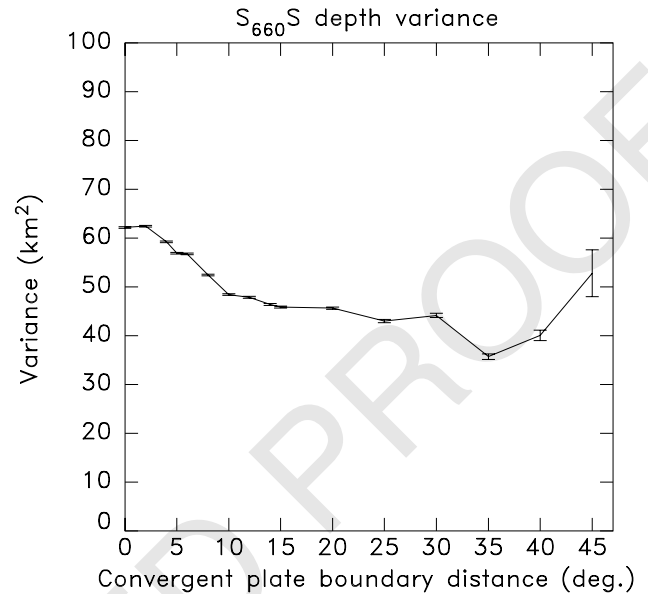
Figure 7. Calculated variance in 660 km discontinuity depth using corrected cap-averaged depths reported by (Flanagan & Shearer 1998), excluding data points close to convergent plate boundaries. The horizontal axis gives the exclusion distance. Uncertainties of the calculated variances were obtained by jackknifing the observational data, and roughly scale as $1/N$, where N is the number of point estimates. The variance falls to low levels when points closer than 14° from a subduction zone are excluded, suggesting a minor, but detectable influence of slabs on the 660 km *SS* precursor signal.

tains any signal related to plumes. We expect plume conduits to be narrow because hotspot tracks on the oceanic lithosphere are narrow, and for fluid mechanical reasons (Sleep 1992), so any plume contribution would be at short correlation lengths (around 2°–3°). This is smaller than both the bin size and the smoothing applied to the discontinuity topography, so we estimate $c(\theta)$ at small separations again by assuming that it decays exponentially from its maximum. At $\theta = 2°$–3°, the approximate plume conduit radius in the lower mantle, $c(\theta)$ is 0.80–0.68, leading to a 36–31 km^2 variance for this process, or 5.6–6 km for the topography. Accounting for the uplift bias factor of ≈ 4, this yields 22.4–24.0 km of topography possibly caused by plumes. This requires temperature variations of 160 K to account for correlations on the scale of plume conduit widths. This value is somewhat smaller than the 200–250 K temperatures estimated geochemically or from bathymetric anomalies near hotspots (Schilling 1991; Sleep 1992).

5.2 Middle and bottom of the lower mantle

There is no opportunity to corroborate tomographic estimates of thermal variations in the deeper reaches of the lower mantle with discontinuity behaviour, and the agreement achieved at the top of the lower mantle suggests there may be a factor of 2 uncertainty in the estimation. In the mid-mantle, seismic wave speed variations from a reference model translate into ± 60 K lateral temperature variations at characteristic spatial scales of 7° (for *P*) and 9° (for *S*). To verify that these temperature differences lead to a physically plausible mid-mantle behaviour, one may treat the region with the thermal anomaly as a Stokes body, the characteristic buoyant movement speed of which is

8   *G. Helffrich*

$$v = \frac{g \Delta \rho d^2}{18 \eta}, \tag{5}$$

where g is the gravitational acceleration (9.8 m s^{-2}), $\Delta \rho$ is the density difference (3.6 kg m^{-3} for a ± 60 K thermal anomaly in the mid-mantle), d is the diameter of the region (7°–9°, corresponding to 595–765 km in mid-mantle) and η is the viscosity of the lower mantle, $\approx 10^{21}$ Pa s. The characteristic rising or sinking speed is 2.9 cm yr^{-1}, which is close to average convective speeds in the mantle, 2.2–3.7 cm yr^{-1} (van Keken & Zhong 1999).

P- and S-wave speed variations are remarkably different at the bottom of the mantle (see Figs 3 and 4), probably indicating an origin that is not exclusively thermal—compositional differences or the presence of melt probably contribute to the signal. To heat or cool material near the CMB enough to generate the P- and S-wave speed variations, one needs lateral temperature differences of at least ± 60 and ± 300 K. Coupled with different correlation lengths (14° and 24° for P and S), the process leading to variations in P-wave speeds is probably not the same as it is for S.

Richards *et al.* (1988) and Ribe & de Valpine (1994) analysed hotspot positions and found non-random correlation at spherical harmonic degrees one and two. In the latter work, they inferred that this spacing represented the fastest-growing convective instability at the CMB, which eventually expresses itself as a plume. We find supportive evidence for this structure in the P- and S-wave speed angular correlation functions at the CMB, but not at other levels in the mantle. The temperature differences that give rise to the degree-two pattern, however, are even lower than the 300 K estimated from the S angular correlation function because it is smaller than e^{-1}. Thus the results suggest that small temperature differences at the CMB might drive the part of the degree-two convective instability visible to delay-time tomography, but, given the evidence for non-thermal contributions to CMB wave speeds and the limitations of the approach initially discussed, they are not resolved very well.

6 CONCLUSIONS

The minerals making up the Earth's mantle provide two ways to examine temperature variations at depth in the mantle. One way is to look at variations in seismic wave speeds relative to a velocity reference model, and interpret them as being caused by temperature changes. Another way is to use the change in depth of a seismic discontinuity to a change in temperature in the mantle through the Clapeyron slope dP/dT of the mineralogical reaction causing the discontinuity. As an experiment in a statistical approach to analyse seismological data sets, we used the angular correlation function of tomographic P- and S-wave speed variations, and the topography of the 660 km seismic discontinuity to extract temperatures at the characteristic length-scales where variations are correlated. The outcome is not resoundingly successful. At the top of the lower mantle, where both ways may be used to estimate lateral variations in mantle temperatures, they disagree. Wave speed variations suggest ± 60 K temperature changes, while the 660 km discontinuity depth variations are attained with temperatures varying by ± 120 or ± 90 K if the influence of subduction zones is removed. To achieve even this factor of 2 level of agreement requires substantial corrections for the bias in the way that SS samples the discontinuities. In the middle of the lower mantle, seismic wave speed variations suggest ± 60 K temperature variations, but the only consistency check is that the P and S waves yield similar results: they do. Moreover, the thermal anomaly and length-scale obtained yield reasonable estimates for mid-mantle convective velocities, ≈ 2.9 cm yr^{-1}, close

to those obtained through convection simulations. At the bottom of the lower mantle, seismic wave speed variations in P and S differ dramatically in magnitude and lateral scale, suggesting that they do not share a common origin. At least ± 60 K variation in temperature is required at the bottom of the mantle to explain P-wave speed variations, and $\pm 300°$ to explain S. However, both tomographic data sets show a degree-two pattern at the CMB, and negatively correlated wave speeds in a band of $\pm 45°$ (for P) and $\pm 30°$ (for S) at 90°.

The principal impediment to analysing global data sets through its angular correlation function is its underlying gridding. The spatial scales of geological structures in the mantle, the influence of which one seeks in the data, are 100–200 km. Coarser grids mask these interesting wavelengths. It would help to have finer gridding with gaps where data coverage is absent, rather than coarser grids with data throughout. Perhaps two gridding levels could be provided, one for uniform coverage, and another for spatial scale investigation.

For the particular goal of determining lateral temperature variations in the mantle, were a well-understood phase change is found to occur near the CMB, the deflection of the associated seismic discontinuity in D″ would provide a way to assess the thermal contribution to lowermost mantle wave speed variations. This is probably the only other level in the lower mantle that might admit to interrogation through an analysis of discontinuity topography, since it otherwise seems to lack global discontinuities.

REFERENCES

Anderson, O.L., Isaak, D.L. & Oda, H., 1991. Thermoelastic parameters for six minerals at high temperature, *J. geophys. Res.,* **96,** 18 037–18 046.

Bina, C.R. & Helffrich, G.R., 1992. Calculation of elastic properties from thermodynamic equation of state principles, *Annu. Rev. Earth Planet. Sci.,* **20,** 527–552.

Bina, C.R. & Helffrich, G.R., 1994. Phase transition Clapeyron slopes and transition zone seismic discontinuity topography, *J. geophys. Res.,* **99,** 15 853–15 860.

Chaljub, E. & Tarantola, A., 1997. Sensitivity of SS precursors to topography on the upper-mantle 660 km discontinuity, *Geophys. Res. Lett.,* **24,** 2613–2616.

Chopelas, A., Boehler, R. & Ko, T., 1994. Thermodynamics and behavior of γ-Mg$_2$SiO$_4$ at high pressure: Implications for Mg$_2$SiO$_4$ phase equilibrium, *Phys. Chem. Minerals,* **21,** 351–359.

Dziewonski, A. & Woodhouse, J., 1987. Global images of the earths interior, *Science,* **236,** 37–48.

Fei, Y., Mao, H.K. & Mysen, B.O., 1991. Experimental determination of element partitioning and calculation of phase relations in the MgO–FeO–SiO$_2$ system at high-pressure and high-temperature, *J. geophys. Res.,* **96,** 2157–2169.

Flanagan, M.P. & Shearer, P.M., 1998. Global mapping of topography on transition zone velocity discontinuities by stacking SS precursors, *J. geophys. Res.,* **103,** 2673–2692.

Furukawa, Y., 1994. Two types of deep seismicity in subducting slabs, *Geophys. Res. Lett.,* **21,** 1181–1184.

Gale, J., 1997. GULP: a computer program for the symmetry-adapted simulation of solids, *J. Chem. Soc., Faraday Trans.,* **93,** 629–637.

Garnero, E.J., Revenaugh, J., Williams, Q., Lay, T. & Kellogg, L.H., 1998. Ultralow velocity zone at the core–mantle boundary, in *The Core–Mantle Boundary Region,* pp. 319–334, eds Gurnis, M., Wysession, M.E., Knittle, E. & Buffett, B., Am. geophys. Un., Washington, DC.

Grand, S.P., 1994. Mantle shear structure beneath the Americas and surrounding oceans, *J. geophys. Res.,* **99,** 11 591–11 621.

Helffrich, G.R., 2000. Topography of the transition zone seismic discontinuities, *Rev. Geophys.,* **38,** 141–158.

Helffrich, G. & Wood, B., 2001. The Earth's mantle, *Nature,* **412,** 501–507.

Ita, J. & Stixrude, L., 1992. Petrology, elasticity and composition of the mantle transition zone, *J. geophys. Res.,* **97,** 6849–6866.

Jaupart, C., Mareschal, J.C., Guillou-Frottier, L. & Davaille, A., 1998. Heat flow and thickness of the lithosphere in the Canadian Shield, *J. geophys. Res.,* **103,** 15 269–15 286.

Jenkins, G.M. & Watts, G., 1968. *Spectral Analysis and its Applications,* Holden-Day, San Francisco, CA.

Kaneshima, S. & Helffrich, G., 1999. Dipping low velocity layer in the mid-lower mantle: evidence for geochemical heterogeneity and ancient oceanic crust, *Science,* **283,** 1888–1891.

Karki, B.B., Stixrude, L. & Crain, J., 1997. *Ab initio* elasticity of three high-pressure polymorphs of silica, *Geophys. Res. Lett.,* **24,** 3269–3272.

Kennett, B.L.N., Widiyantoro, S. & van der Hilst, R.D., 1998. Joint seismic tomography for bulk sound and shear wave speed in the Earth's mantle, *J. geophys. Res.,* **103,** 12 469–12 493.

Kesson, S., Gerald, J.D.F. & Shelley, J., 1998. Mineralogy and dynamics of a pyrolite lower mantle, *Nature,* **393,** 252–255.

Kincaid, C. & Silver, P.G., 1996. The role of viscous dissipation in the orogenic process, *Earth planet. Sci. Lett.,* **142,** 271–288.

Knittle, E. & Jeanloz, R., 1991. Earth's core–mantle boundary—results of experiments at high-pressures and temperatures, *Science,* **251,** 1438–1443.

Larson, R.L. & Olson, P., 1991. Mantle plumes control magnetic reversal frequency, *Earth planet. Sci. Lett.,* **107,** 437–447.

Levi, B.L., 1992. COBE measures anisotropy in cosmic microwave background radiation, *Phys. Today,* **45,** 17–20.

Loper, D.E. & Lay, T., 1995. The core–mantle boundary region, *J. geophys. Res.,* **100,** 6397–6420.

Neele, F., de Regt, H. & VanDecar, J., 1997. Gross errors in upper-mantle discontinuity topography from underside reflection data, *Geophys. J. Int.* **129,** 194–204.

Peebles, P.J.E., 1980. *The Large-Scale Structure of the Universe,* Princeton University Press, Princeton, NJ.

Ribe, N.M. & de Valpine, D.P., 1994. The global hotspot distribution and instability in D″, *Geophys. Res. Lett.,* **21,** 1507–1510.

Richards, M.A., Hager, B.H. & Sleep, N.H., 1988. Dynamically supported geoid highs over hotspots: observation and theory, *J. geophys. Res.,* **93,** 7690–7708.

Saxena, S., Dubrovinsky, L., Lazor, P., Cerenius, Y., Haggkvist, P., Hanfland, M. & Hu, J., 1996. Stability of perovskite (MgSiO$_3$) in the Earth's mantle, *Science,* **274,** 1357–1359.

Schilling, J.-G., 1991. Fluxes and excess temperatures of mantle plumes inferred from their interaction with migrating mid-ocean ridges, *Nature,* **352,** 397–403.

Serghiou, G., Zerr, A. & Boehler, R., 1998. (Mg, Fe)SiO$_3$-perovskite stability under lower mantle conditions, *Science,* **280,** 2093–2095.

Shearer, P.M., 1993. Global mapping of upper-mantle reflectors from long-period *SS* precursors, *Geophys. J. Int.* **115,** 878–904.

Sleep, N.H., 1992. Hotspot volcanism and mantle plumes, *Annu. Rev. Earth planet. Sci.,* **20,** 19–43.

Su, W.-J. & Dziewonski, A., 1992. On the scale of mantle heterogeneity, *Phys. Earth planet. Inter.,* **74,** 29–54.

van der Hilst, R.D., Engdahl, E.R. & Spakman, W., 1993. Tomographic inversion of *P* and *pP* data for aspherical mantle structure below the northwest pacific region, *Geophys. J. Int.* **115,** 264–302.

van der Hilst, R.D., Widiyantoro, S. & Engdahl, E.R., 1997. Evidence for deep mantle circulation from global tomography, *Nature,* **386,** 578–584.

van Keken, P. & Zhong, S., 1999. Mixing in a 3D spherical model of present-day mantle convection, *Earth planet. Sci. Lett.,* **171,** 533–547.

Weinstein, S.A. & Olson, P.L., 1989. The proximity of hotspots to convergent and divergent plate boundaries, *Geophys. Res. Lett.,* **16,** 433–436.

Zerr, A., Diegeler, A. & Boehler, R., 1998. Solidus of Earth's deep mantle, *Science,* **281,** 243–246.